

GPPS-TC-2021-0341

ASSESSMENT OF RANS AND SBES METHODS FOR THE PREDICTION OF CORNER SEPARATION IN AXIAL FLOW COMPRESSORS

Wei Sun
Aero Engine Academy of China
swsunwei000000@163.com
Beijing, China

ABSTRACT

Corner separation is a common three-dimensional (3D) separated flow presented at the junction of the blade suction surface and endwall within axial-flow compressors. One commonly used Reynolds-Averaged Navier-Stokes (RANS) turbulence model in turbomachinery Computational Fluid Dynamics (CFD) simulations, Menter's Shear Stress Transport (SST) model, usually struggles to predict corner separation and its impact on compressor performance with reasonable accuracy.

To improve RANS modelling accuracy for corner separation, efforts have been focused on the modifications of SST model in order for more of the endwall flow physics to be captured, such as the increased turbulence non-equilibrium and anisotropy due to the generation of skew-induced streamwise vortices in the endwall secondary flow.

In this paper, the effect of the non-equilibrium and anisotropic modifications on the prediction of corner separation is evaluated using the results of the SST model and its variants. A high-fidelity time-accurate turbulence statistics database constructed by a newly developed hybrid RANS-Large Eddy Simulation (RANS-LES) method, Stress-Blended Eddy Simulation (SBES), is then used to feedback on RANS modelling. The investigation of the scale resolved corner flow physics facilitates understanding the physical reasons underlying the increased modelling accuracy of corner separation, in the meantime it reveals the modelling deficiencies that still exist.

INTRODUCTION

Corner separation is one common 3D flow phenomenon in axial-flow compressors that can significantly affect the compressor performance (Denton, 2010; Gourdain et al., 2014). When a multi-stage compressor is operating away from its intended design condition, the flow becomes increasingly complex, and large-scale, localized corner separations will be presented in the area close to the endwall in blade-row passages. The RANS-based modelling approaches, currently the mainstream tools affordable to industry, are usually found to over-predict the blockage and loss due to corner separation (Bush et al., 2019). The predictive discrepancy of the blockage due to separation in one blade row can ultimately lead to exacerbation of stage-loading mismatches throughout the whole compressor. Hence, in order for the RANS CFD to serve as a reliable flow simulation tool in the compressor design iterations, it is necessary for the RANS turbulence models to predict corner separation and its impact on compressor performance with good accuracy.

To dig out the sources of RANS modelling uncertainty for corner separation, the compressor endwall flow features are reviewed. This would help to understand the differences between the flow features which RANS models aim to capture and the real endwall flow features which are critical and the models need to capture.

Corner separation in compressors arises as a result of a combined effect of diffusion and endwall flow over-turning (Goodhand, 2011). Diffusion arises due to increased passage flow area, making both the endwall and the blade surface boundary layers prone to separation. Meanwhile, under the effect of both the adverse streamwise pressure gradient and transverse pressure gradient, the endwall boundary layer with low streamwise momentum is convected across the passage and impinges on the blade suction surface. Gbadebo et al. state that "The interaction of the weakened boundary layers under the adverse pressure gradient with the secondary flow results in the 3D nature of separation" (Gbadebo et al., 2007). This can be understood as that an injection of the endwall fluid with low streamwise momentum into the suction surface boundary layer forms the origin of separation and yields a 3D flow structure referred to as corner separation. Thus, the complexity of the compressor endwall flow is mainly reflected in the three aspects: 1) endwall secondary flow upstream of corner separation, 2) endwall/blade boundary layer under the streamwise adverse pressure gradient, and 3) free shear layer flow within the corner separation region.

In the endwall flow region which is upstream of corner separation, the boundary layer is skewed due to overturning of the fluid close to the endwall from pressure to suction side. The skewness not only changes the strength of turbulent shear inside the endwall boundary layer, but induces a skewed vorticity sheet with changing directions. Both the change

in velocity gradient and that in vorticity gradient contribute to creating more turbulence mixing so it shall be a combined effect of higher turbulence production and increased turbulence anisotropy due to generation of skew-induced streamwise vortices. The commonly used RANS turbulence models in industrial CFD simulations, e.g., Menter's SST model, were formulated based on simplified assumptions on turbulence energy equilibrium and isotropic distribution of the turbulence intensity (Menter et al., 2003). This indicates that the turbulence behaviours in the 3D skewed wall shear layers cannot be predicted by the SST model with reasonable accuracy.

Once the wall shear layer separates, the separated flow is subjected to 3D shear in the free space around the corner. It is highly swirling and unsteady, with the turbulence characteristics of which being non-equilibrium and anisotropic (Liu et al., 2011; Wang et al., 2013). The RANS turbulence models, which were formulated based on the assumption on the turbulence energy equilibrium in 2D wall shear layers and the Boussinesq hypothesis regarding the Reynolds stress-strain constitutive relation, are difficult to predict the corner separation flow with reasonable accuracy.

To increase the RANS modelling accuracy of corner separation, a series of studies have focused on formulating the turbulence equation source terms and the nonlinear Reynolds stress-strain constitutive relation, e.g., Menter et al. (2018), Liu et al. (2019), and Sun et al. (2020). For Liu et al.'s SST model with helicity correction (SST-Helicity), the production terms in both turbulence equations are modified by using the normalized velocity helicity to model the turbulence energy backscatter physics, which can be significant in the corner separation (Liu et al., 2011). This modification is expected to significantly improve the prediction accuracy of complex 3D vortical flows, such as the compressor corner separation. While in canonical flows that have been validated for the SST model, the modification will automatically switch off to zero because velocity helicity is zero (Liu et al., 2019). For Sun et al.'s SST model without stress limiter (NSST), the stress limiter is removed from the eddy-viscosity definition to avoid the unphysical restriction of the growth of eddy viscosity in non-equilibrium boundary layers, where turbulence non-equilibrium is caused by skewness rather than the abrupt change in the mean strain rate. For Menter et al.'s SST model with explicit anisotropic correction (SST-QCR), adding the quadratic strain-vorticity term to the Boussinesq constitutive relation increases the Reynolds stress anisotropy, which induces the secondary flow of the second kind around the corner. The secondary flow of the second kind extracts high-momentum fluid from the main passage into the corner flow region, thus energizing corner flow to be resistant to separation (Sun and Xu, 2021).

Based on previous studies on the non-equilibrium and anisotropic modelling for compressor flows, the objective of this paper is two fold: one is to study which extent the above SST model variants reproduce the corner separation flow physics, and another is to provide an "optimal" SST-type model for the prediction of corner separation. To achieve this objective, first, the impact of the non-equilibrium and anisotropic modifications on the corner separation prediction is evaluated by analyzing the prediction results of SST model variants for the LMFA-NACA65 compressor cascade flows under various inflow conditions. A high-fidelity time-accurate turbulence database constructed by SBES is then used to feedback on RANS modelling. The scale resolved endwall flow physics are studied to confirm that improved SST model variants have been developed, in the meantime to reveal the modelling deficiencies that still exist.

MODEL FORMULATION

In this section, Menter's SST model and its variants are presented and discussed. Then, the SBES method is briefly introduced, with its advantages over the conventional hybrid RANS-LES approaches summarised. For brevity purposes, only the key variables and terms are explained in this section.

Menter's SST 2003 Model (SST 2003)

$$\frac{\partial k}{\partial t} + \frac{\partial(u_j k)}{\partial x_j} = \widetilde{P}_k - \beta^* k \omega + \frac{\partial}{\partial x_j} \left[(v + \sigma_k v_t) \frac{\partial k}{\partial x_j} \right] \quad (1)$$

$$\frac{\partial \omega}{\partial t} + \frac{\partial(u_j \omega)}{\partial x_j} = \frac{\gamma}{v_t} \widetilde{P}_k - \beta \omega^2 + \frac{\partial}{\partial x_j} \left[(v + \sigma_\omega v_t) \frac{\partial \omega}{\partial x_j} \right] + 2(1 - F_1) \frac{\sigma_{\omega 2}}{\omega} \frac{\partial k}{\partial x_j} \frac{\partial \omega}{\partial x_j} \quad (2)$$

where the turbulence kinetic energy (TKE) production term \widetilde{P}_k is defined as:

$$\widetilde{P}_k = \min \left(\tau_{ij} \frac{\partial u_i}{\partial x_j}, 10 \beta^* k \omega \right) \quad (3)$$

where τ_{ij} is the Reynolds stress tensor and is calculated using the Boussinesq hypothesis for the Reynolds stress-strain constitutive relation (see in the expression of τ_{ij}^{EV} in Equation (9)). The TKE production limiter in the right-hand side of Equation (3) does not affect the shear layer performance but avoids buildup of TKE around the stagnation point in aerodynamic applications (Menter et al., 2003).

The first three source terms in the right-hand side of Equation (1) and (2) represent the production, dissipation, and diffusion terms of k and ω , respectively. The fourth term in the right-hand side of Equation (2) is the cross-diffusion

term generated by transforming $k-\varepsilon$ model to its $k-\omega$ formulation, and F_1 is the blending function used to blend $k-\varepsilon$ model and $k-\omega$ model in the boundary layer wake region (Menter, 1994). In the logarithmic layer and below, $F_1=1$, and the original $k-\omega$ model recovers; from the logarithmic layer up to the freestream, F_1 tends to be 0, so that the SST model turns to be the $k-\omega$ formulation of $k-\varepsilon$ model.

The turbulent eddy viscosity is computed from (Menter et al., 2003):

$$\mu_t = \min \left[\frac{\rho k}{\omega}, \frac{\rho a_1 k}{SF_2} \right] \quad a_1 = 0.31 \quad (4)$$

where $\rho a_1 k / SF_2$ is the stress limiter, and F_2 is a blending function which remains as one across most area of the boundary layer, while falling off rapidly to zero at the edge of the boundary layer. This means that the stress limiter only serves to limit the growth of eddy viscosity inside the boundary layer. The F_2 function reads as follows (Menter, 1994):

$$F_2 = \tanh \left\{ \left[\max \left(\frac{2\sqrt{k}}{\beta^* \omega d}, \frac{500\nu}{d^2 \omega} \right) \right]^2 \right\} \quad (5)$$

Menter's SST 2003 with Helicity (SST 2003-Helicity)

In Menter's SST 2003 model with helicity, the TKE production term \widetilde{P}_k in both Equation (1) and (2) is modified by adding a source term to \widetilde{P}_k . The added source term represents the effect of the turbulence energy backscatter on the TKE production and is termed as \widetilde{P}_{kh} in the below (Liu et al., 2019).

$$\widetilde{P}_{kh} = \nu_t (c_{h1} h^{c_{h2}}) \Omega^2 \quad c_{h1} = 0.71 \quad c_{h2} = 0.6 \quad (6)$$

where h is the absolute value of the relative helicity density, and is defined as:

$$h = \left| \frac{\vec{v} \cdot \vec{\omega}}{|\vec{v}| |\vec{\omega}| + 0.00001} \right| \quad (7)$$

where \vec{v} is the velocity vector, $\vec{\omega}$ the vorticity vector, 0.00001 m/s^2 added in the denominator to avoid division by zero. $(c_{h1} h^{c_{h2}})$ characterizes the effect of the turbulence energy backscatter on the turbulence production in the corner separation region (Liu et al., 2011). This indicates that in the corner separation where the turbulence energy backscatter is significant ($h > 0$), the turbulence production is increased to model the energy cascade from smaller scales of turbulence to large scales.

Menter's SST 2003 without Stress Limiter (NSST)

In Menter's SST 2003 model without stress limiter, the stress limiter is removed from the eddy viscosity definition (Equation (4)) to model the non-equilibrium behaviours of turbulence in skewed wall shear layers (Sun et al., 2020). The eddy viscosity in the NSST model is expressed as:

$$\mu_t = \frac{\rho k}{\omega} \quad (8)$$

This modification has shown wide applicability in the prediction of endwall flow in compressors (Sun, 2021).

Menter's Explicit Quadratic Constitutive Relation ($k-\omega$ type models-QCR)

By including the second-order tensor scalar product terms (i.e., the quadratic strain-vorticity terms), this relation is a quadratic extension over the Boussinesq linear Reynolds stress-strain relation, and is expressed as (Menter et al., 2018):

$$\tau_{ij} = \tau_{ij}^{EV} - C_{CORNER} \frac{1.2\nu_t}{\max \left(0.3\omega, \sqrt{0.5(S^2 + \Omega^2)} \right)} (S_{ik}\Omega_{kj} - \Omega_{ik}S_{kj}) \quad \tau_{ij}^{EV} = -\frac{2}{3}k\delta_{ij} + 2\nu_t S_{ij} \quad (9)$$

As shown in Equation (9), the Menter's explicit Reynolds stress-strain relation was designed to be coupled with the ω type two-equation models to close the RANS governing equations. In this paper, QCR is coupled with the SST model and its variants, so as to capture the anisotropic turbulence physics around the corner region.

SBES Method

The principle of SBES is quite similar to that of the conventional Detached Eddy Simulation (DES)-type approaches (Spalart, 2009), which were all designed to cover the attached boundary layers by RANS and to only switch to LES in flow detached regions. However, compared with DES and its variants, SBES has shown significant advantages, which is mainly reflected in the following three aspects:

- 1) SBES allows for more rapid switchover from RANS to LES once flow separates. This is achieved by the grid filter width defined in SBES;
- 2) An enhanced RANS-LES blending function was designed to ensure robust shielding of the attached boundary layers by the RANS portion of SBES. This reduces the sensitivity of SBES to mesh densities as in the hybrid RANS-LES context, the near-wall mesh is not dense enough to sustain resolved turbulence;
- 3) RANS and LES can be hybridized by zonal and/or global blending functions, which allows for the free choice of LES subgrid-scale (SGS) models, rather than rely on the Smagorinsky model. The RANS and LES regions can also be distinguished by the blending function.

In light of the SBES advantages and the computational resources available, SBES was chosen to construct the scale-resolving compressor flow database. This database was then used to evaluate the capability of SST and its model variants to capture the corner separation flow physics.

COMPUTATIONAL SET-UP

In this section, the computational models and CFD solver that are used in the current research are briefly introduced. The LMFA-NACA65 compressor cascade (Ma, 2012; Zambonini, 2016) and the Prescribed Velocity Distribution (PVD) compressor cascade (Gbadebo et al., 2005) are used as computational models. For LMFA-NACA65 compressor cascade, the experimental data of flow at various inlet conditions (inlet flow incidences 0° , 2° , 4°) is accessible and used for model validation. The PVD cascade was specifically designed and experimentally measured for investigation into the formation and control of 3D separations in axial compressors (Gbadebo, 2004). The SBES results of the PVD cascade flow are used to investigate the corner separation flow physics, and feedback on RANS modelling.

Flow Solver

Both RANS and SBES simulations are performed using ANSYS FLUENT 19.2, where model modifications were implemented through user-defined macros. For RANS simulations, the default second-order upwind scheme is chosen for spatial discretization of the convection terms in all transport equations; for the SBES simulation, the bounded central-differencing scheme is chosen for discretization of the convection terms, so as to achieve low numerical dissipation in the LES zone. The bounded central-differencing scheme can also handle the RANS zone and RANS-LES interface zone with reasonable accuracy (Menter, 2015).

LMFA-NACA65 Compressor Cascade

On the LMFA-NACA65 compressor cascade test rig, 13 NACA65-009 airfoils were installed at the end of an open-circuit subsonic wind tunnel (Ma, 2012). During the test, two strips of sandpaper were separately stuck on the blade suction surface and pressure surface. The sandpaper was located at an arc length of 6mm from the leading edge, with the aim of triggering transition at the initial phase of blade surface boundary layer development. This eliminates the influence of upstream transition on corner separation and reduces the RANS difficulties, as no transition is needed to be modelled by RANS.

Mesh

Figure 1 shows the CFD domain and grid topology of LMFA-NACA65 cascade. An H-O-H grid topology is used to ensure grid orthogonality (Figure 1a), and hexahedral structural cells are generated using NUMECA Autogrid^{v8} (Figure 1b). Within O block, 396 points are wrapped around the blade and 73 points are distributed in the wall-normal direction above the blade surface, with the average y^+ around 0.8 and grid expansion ratio less than 1.2. In the spanwise direction, 93 points are placed, with the maximum y^+ around 1.0 and grid expansion ratio less than 1.2 as well. The overall mesh consists of around 3.32 million cells, of which is fine enough with respect to the grid density requirements for RANS simulations (Sun, 2021).

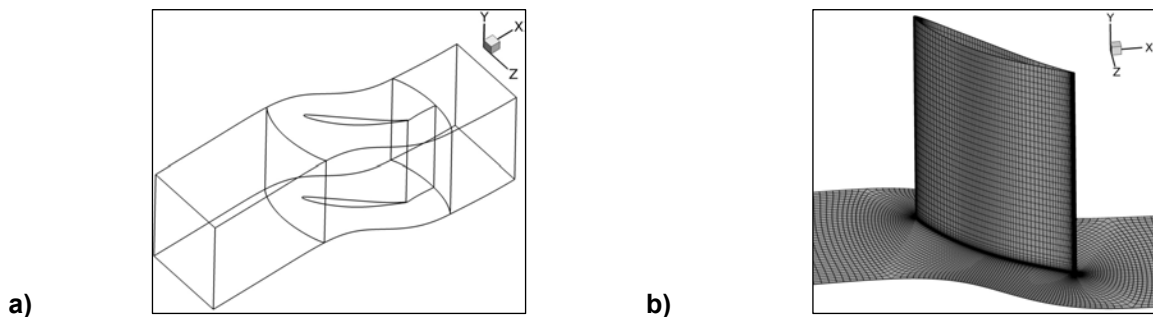


Figure 1: Computational domain of the LMFA-NACA65 cascade. (a) mesh topology, (b) mesh distribution (every 2nd grid point shown for visual clarity).

Boundary Conditions

The mean-flow boundary conditions are specified to correspond to the experimental conditions, including the inlet mean velocity profile, inflow direction, static temperature, density, and the outlet mean static pressure. The inlet mean velocity profile was obtained through RANS simulation for the zero-pressure-gradient flat-plate turbulent boundary layer, with the result of which matching the hotwire measurements of the cascade inlet endwall boundary layer.

As for the inlet turbulence boundary conditions, no detailed measurement results of the fluctuating velocities inside the endwall boundary layer are available. There thus inevitably exist some uncertainties in the setting of inlet turbulence conditions. In the current study, the extracted mean velocity profile and the corresponding turbulent variable profiles (i.e. TKE k and specific dissipation rate ω), are specified on the cascade inlet boundary zone.

PVD Compressor Cascade

The PVD compressor cascade consists of five controlled diffusion blades, which are typical of high-pressure stator blades in turbofan engines (Gbadebo, 2004). The computational domain of the PVD cascade is shown in Figure 2, with the full-span simulations conducted by both RANS and SBES.

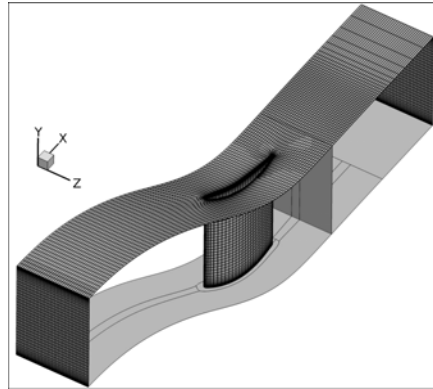


Figure 2: Computational domain of the PVD cascade. (every 4th grid point shown for visual clarity).

Mesh

An O4H grid topology is adopted, and hexahedra grid cells are generated using NUMECA Autogrid^{®8}. The following non-dimensional near-wall grid spacings are used, based on the wall-friction velocity u_τ at inlet:

- Blade surface: $\Delta x^+ < 120$ (streamwise), $y^+ < 1$ (wall-normal), $\Delta z^+ < 110$ (spanwise);
- Endwall: $\Delta x^+ < 120$ (streamwise), $y^+ < 1$ (wall-normal), $\Delta z^+ < 60$ (pitchwise).

The grid spacings above lead to 274 points wrapped around the blade surface, 257 points distributed along the blade span with clustering near the endwall, and the near-wall grid expansion ratio being about 1.1. In the separation region, the isotropic meshes, with aspect ratio less than 2, were designed to better resolve the large-scale turbulence structures in the LES mode. Overall, the total cell count is about 19 million.

Boundary Conditions

The SBES boundary conditions are specified to match the experimental conditions, and are listed as follows:

- The inlet conditions of SBES comply with those of RANS, with both assuming the inlet endwall boundary layer being fully turbulent. In RANS and SBES simulations, the inlet endwall boundary layer is modelled by RANS and SBES RANS mode, respectively;
- For the inlet turbulence injection, with the measured inlet freestream turbulence intensities being quite low (1.5%), no turbulence injection methods were applied in the LES region of inlet. Furthermore, this separation is kind of insensitive to the inlet freestream turbulence, due to the instability largely driven by the endwall&blade boundary layer thickness and the adverse streamwise pressure gradient;
- At outlet, the mean static pressure is specified in accordance with the experimental condition. A non-reflecting condition is also specified at outlet to damp out the spurious wave reflections from the outlet boundary into the interior domain.

Temporal Discretization

The FLUENT's implicit dual-time stepping method is used in the SBES simulation, with the second-order backward Euler scheme in the physical time-marching procedure. The estimate of the physical time step Δt was given by assessing the throughflow time. This is the time required by a fluid element to pass through the LES domain of one blade chord, i.e. T_{tf} (subscript tf short for throughflow). With an estimation of how many cells N are passed by the fluid element, the

physical time step Δt is estimated as $T_{ff}/N \cdot CFL$. By setting CFL as 0.5, the non-dimensional physical time step $\Delta t/T_{ff}$ gives as 3.14×10^{-3} .

As for pseudo (inner) iterations, the maximum number per time step is set as 15, which allows for at least four orders of magnitude drop in the residual level of all flow governing equations at the end per time step, as well as the turbulence closure equations.

All SBES simulations were initialized using the converged steady RANS solution and run for thirty-three through-flow times to flush out the initial transients. The statistics were collected and averaged for further forty-four throughflow times.

MODEL VALIDATION

The validation results for the LMFA-NACA65 compressor cascade flows at two off-design inflow conditions ($i=2^\circ$, 4°) are discussed below. For the design inflow condition ($i=0^\circ$), the NSST-QCR model gives results that closely match the measurements (Sun and Xu, 2021). Detailed studies on the physical reasons for the improvement of corner separation prediction using QCR correction are presented in the author's previous paper (Sun and Xu, 2021).

Case 1 ($i=2^\circ$)

As an illustration of the predicted extent of corner separation, Figure 3 shows the endwall surface limiting streamline distributions computed by SST and its three variants (NSST, SST-Helicity, SST-QCR) at the off-design condition ($i=2^\circ$). An example point on the endwall surface, which is upstream of corner separation, is also selected and shown in Figure 3. The distributions of the TKE production predicted by SST, SST-Helicity, NSST and SST-QCR models are plotted along the endwall-normal cut line from this point outwards (see in Figure 5). It can be shown that compared with the original SST model, the endwall boundary layer predicted by all the three model variants exhibits stronger resistance to bulk adverse pressure gradients when migrating towards the blade suction surface. The separation onset is delayed, and the pitchwise extent of separation is predicted to be smaller. Furthermore, compared with SST with anisotropy correction (SST-QCR), marginal improvement in the control of corner separation size is achieved by SST without stress limiter (NSST) and SST with helicity correction (SST-Helicity).

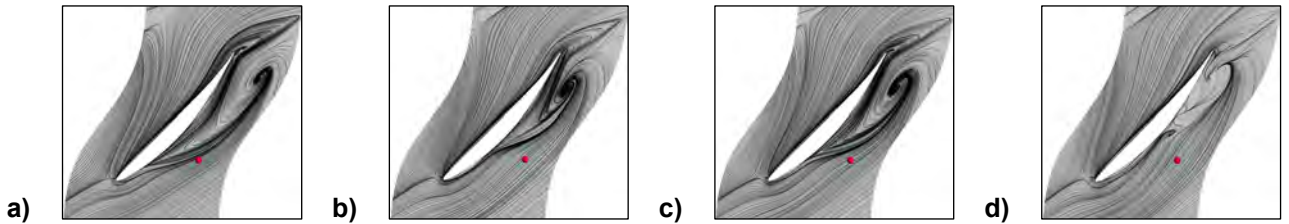


Figure 3: Endwall surface limiting streamlines ($i=2^\circ$), with location of selected point on the endwall surface. (a) SST, (b) NSST, (c) SST-Helicity, (d) SST-QCR.

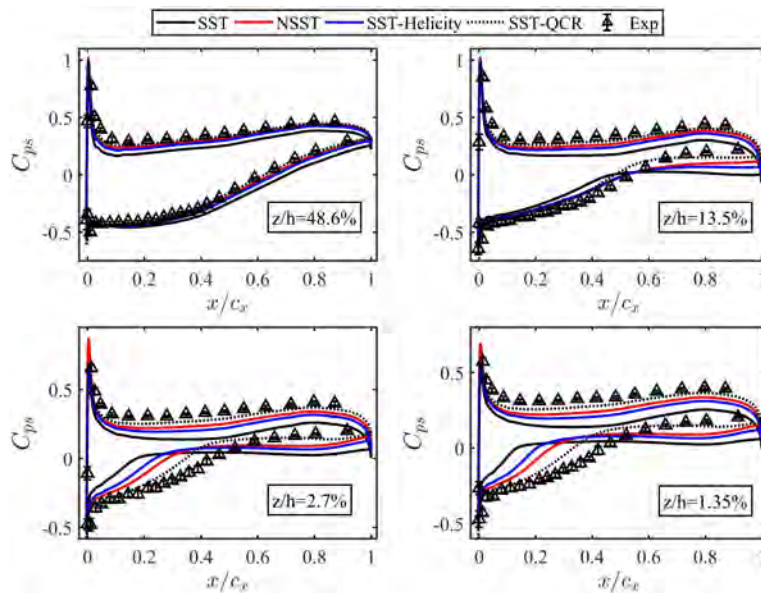


Figure 4: Blade spanwise C_{ps} distributions ($i=2^\circ$). SST variants.

To see how the over-predicted blockage affects blade loading, Figure 4 shows the static pressure distributions on the

blade surface. It can be seen that all three modifications lead to improved predictions of the size of corner separation. Compared with the non-equilibrium modifications (i.e., stress limiter switch-off and helicity correction), the anisotropic modification takes more effect on controlling the unphysical growth of corner separation. The increase in the Reynolds stress anisotropy results in counter-rotating streamwise vortices being generated around the corner, which in turn entrains high-momentum fluid in the main flow into the corner (Sun and Xu, 2021). The corner flow is energized and thus shows stronger resistance to the adverse pressure gradient.

Further, to demonstrate the effect of the non-equilibrium modifications on the prediction of corner separation, Figure 5 shows the distribution of TKE production in the endwall boundary layer upstream of the corner separation, and Figure 6 shows the distribution of the relative helicity density h within the corner separation region.

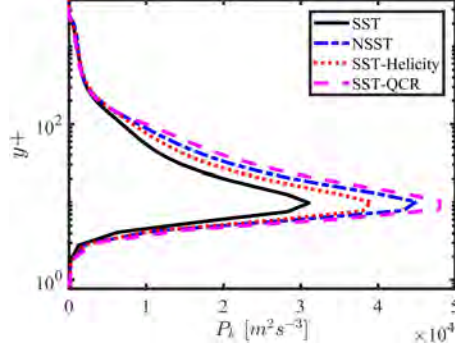


Figure 5: TKE production P_k distribution along the endwall-normal cut line ($i=2$).

As seen in Figure 5, the increase in the TKE production P_k given by SST-QCR and NSST is more significant in the outer layer of endwall boundary layer. As for SST-QCR model, the re-distribution of the Reynolds stresses due to QCR modification induces turbulence non-equilibrium inside the endwall boundary layer, which is achieved by feedback of the modified Reynolds stresses into P_k (see in Equation (3) and (9)). As for NSST model, by switching off the stress limiter in the eddy-viscosity definition, the restriction on the increase of the turbulent shear caused by skewness is lifted, which results in higher P_k inside the endwall boundary layer. This indicates that more intense turbulence momentum transport process is modelled by both SST-QCR and NSST in the outer layer of endwall boundary layer. The endwall boundary layer is energized and migrates further downstream to the suction surface, thus delaying the separation onset. The finding here constitutes one physical reason for the significantly improved predictions of the extent of corner separation by both SST-QCR and NSST.

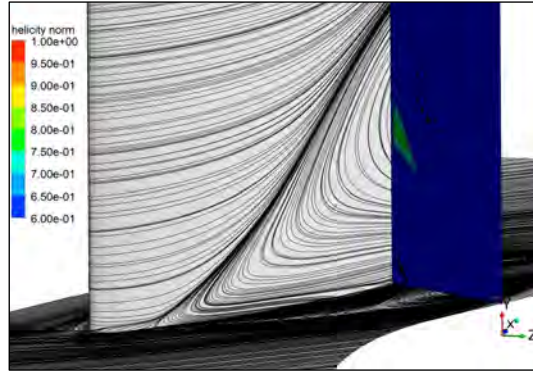


Figure 6: Relative helicity density h within corner separation region in the blade passage ($i=2$).

In contrast, although a significant increase in P_k is achieved by SST-Helicity, its increase value is smaller compared with that by NSST and SST-QCR (see in Figure 5). The helicity modification takes relatively smaller effect on restricting the unphysical growth of corner separation. This is due to the fact that the absolute value of the relative helicity density h is less than 0.6 in most area of the corner separation region (see in Figure 6). As pointed out by Liu et al. (2011), the ratio of turbulence energy backscatter to forward energy dissipation is larger than 1 only when h is more than 0.7. This means that the contribution of the turbulence energy backscatter to the TKE production in the corner separation region is minor, and thus accounts for the relatively minor effect of helicity correction on corner separation in this flow scenario.

Through analysis of the three SST model modifications, it can be seen that each modification attempts to capture part of the endwall flow physics, such as turbulence non-equilibrium (NSST), turbulence anisotropy (QCR), and turbulence energy backscatter (helicity). However, the endwall flow in compressors is a complex physical phenomenon in which the turbulence non-equilibrium, anisotropy and energy backscatter co-exist. This implies that a combination of the “isolated” modifications would be expected to capture more of the endwall flow physics.

Next, the validation results of three combined SST model variants (NSST-Helicity, NSST-QCR and NSST-Helicity-QCR) are discussed, with the aim of developing an “optimal” SST-type model for the corner separation prediction.

Figure 7 shows the blade pressure loading distributions predicted by the NSST-Helicity, NSST-QCR and NSST-Helicity-QCR models. It can be shown that NSST-QCR and NSST-Helicity-QCR almost reproduce the experimental measurements, while a significantly larger corner separation is predicted by NSST-Helicity. This is understandable as at this flow condition, the anisotropic behaviours of turbulence in the endwall region impact more on the development of corner separation (shown in Figure 3 and 4). Compared with NSST-QCR, a slightly better prediction is achieved by NSST-Helicity-QCR, which is reflected in closer match of the predicted blade loading with the measured results.

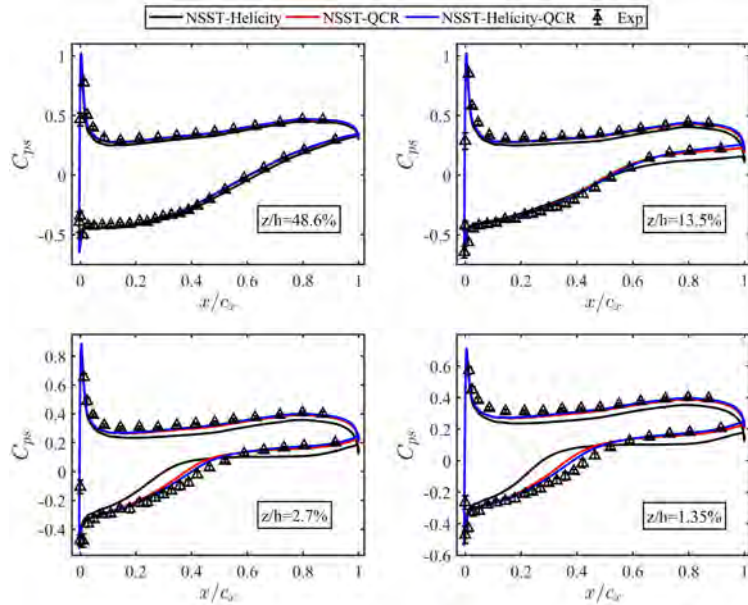


Figure 7: Blade spanwise C_{ps} distributions ($i=2^\circ$). NSST variants.

In summary, the proposed NSST-Helicity-QCR model, which takes account of the turbulence physics as commonly observed in the endwall flow in compressors, has been validated at one off-design flow condition. Next, the generality of NSST-Helicity-QCR for the corner separation prediction is validated by a more challenging test case.

Case 2 ($i=4^\circ$)

Figure 8 compares the blade spanwise pressure loading distributions by NSST-Helicity-QCR with the experimental measurements. It is encouraging to see that the NSST-Helicity-QCR results match closely with measurements, indicating the blockage due to corner separation being reasonably modelled under this flow condition.

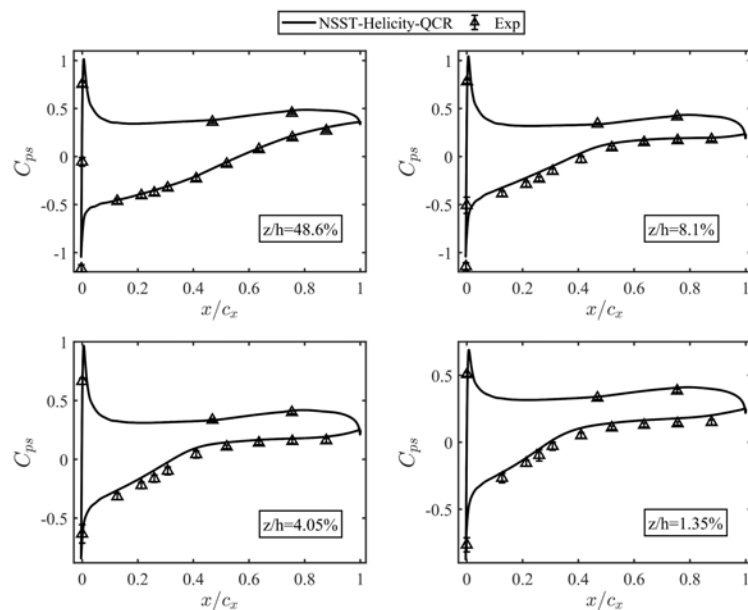


Figure 8: Blade spanwise C_{ps} distributions ($i=4^\circ$). NSST-Helicity-QCR.

As two indexes to measure the extent of the endwall flow blockage, the comparison of the predicted total pressure loss with measurements and that of the predicted exit flow deviation with measurements are shown in Figure 9 and 10.

As Figure 9b shows, the pitchwise mass-averaged total pressure loss coefficient \overline{C}_{pt} predicted by NSST-Helicity-QCR matches closely with the experimental results, despite the predicted size of loss core being significantly larger than the measured (see in Figure 9a). This is also reflected in the exit flow angle distribution near the endwall region (see in Figure 10). The reason for the larger loss core size predicted is that the endwall-flow turbulent diffusion rate predicted by RANS is lower than that in reality. This explains that the loss core size predicted by RANS is larger than that measured, despite the predicted \overline{C}_{pt} being in close proximity to the experimental results.

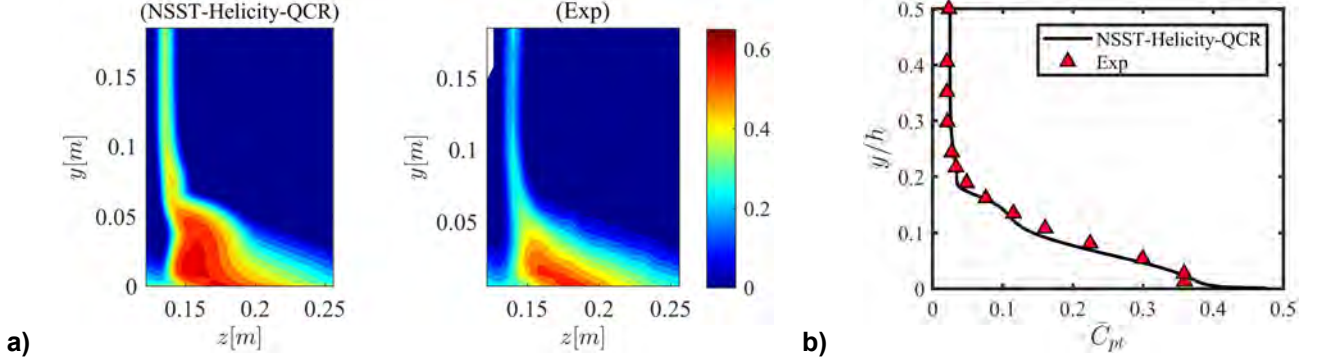


Figure 9: Total pressure loss C_{pt} distribution at section 1 ($x=1.363c_x$, $i=4^\circ$). (a) C_{pt} contour (2D), (b) Pitchwise mass-averaged total pressure loss coefficient \overline{C}_{pt} (1D).

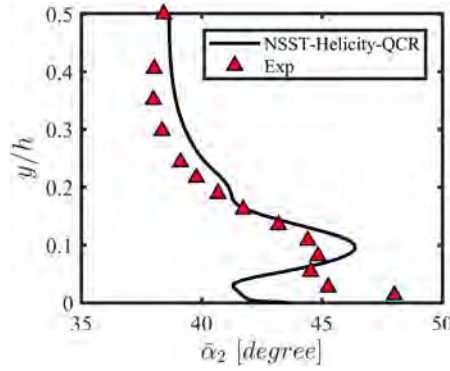


Figure 10: Spanwise distribution of the pitchwise mass-averaged flow angle $\overline{\alpha}_2$ at section 1 ($i=4^\circ$).

In summary, the proposed NSST-Helicity-QCR model possesses high accuracy in predicting corner separation and its impact on compressor performance at various inflow conditions. In the next section, the SBES simulation results for the PVD compressor cascade flow are presented to study the turbulence characteristics of the compressor endwall flow. Through comparison with the SBES results, the capability of NSST-Helicity-QCR model to capture the corner separation flow physics is demonstrated.

SBES RESULTS

In the SBES simulation, the NSST model was chosen as the RANS mode of SBES, and the WALE model (Ducros et al., 1998) was adopted as its LES mode. The selected RANS and LES SGS models were blended by the default blending function (Menter, 2016), and the resulting SBES model is named as SBES-NSST-WALE below.

Unsteady Flowfield

To identify the flow region where is resolved by LES, the SBES blending function is used here. Figure 11 shows the RANS and LES regions on the blade-to-blade plane and the quasi-orthogonal plane normal to the axial direction at one instantaneous time step. Six cut planes are selected and they are shown in Figure 11a. That is, $11\%h$, $19\%h$, $46\%h$ cut planes normal to the spanwise direction; $0.3c_x$, $0.99c_x$, $1.5c_x$ cut planes normal to the axial direction.

As shown from Figure 11b to 11d, when approaching to the endwall, the corner separation region enlarges, and thus more separated flow is resolved by LES. In the boundary-layer flow region upstream of separation, the attached boundary layer is perfectly “shielded” from being contaminated by the LES mode, and thus the grid-induced separation is avoided. Figure 11e shows that the attached boundary layer on both the suction surface and the endwall is shielded by the RANS portion of SBES. When approaching to the edge of boundary layer, smooth transition from RANS to LES is achieved by the blending function. Figure 11f shows that within the separation region, the shielded RANS layer becomes thinner and

more of the separated flow is resolved by LES. Downstream of the trailing edge, as shown in Figure 11g, apart from the region close to the endwall, the whole flow is resolved by LES.

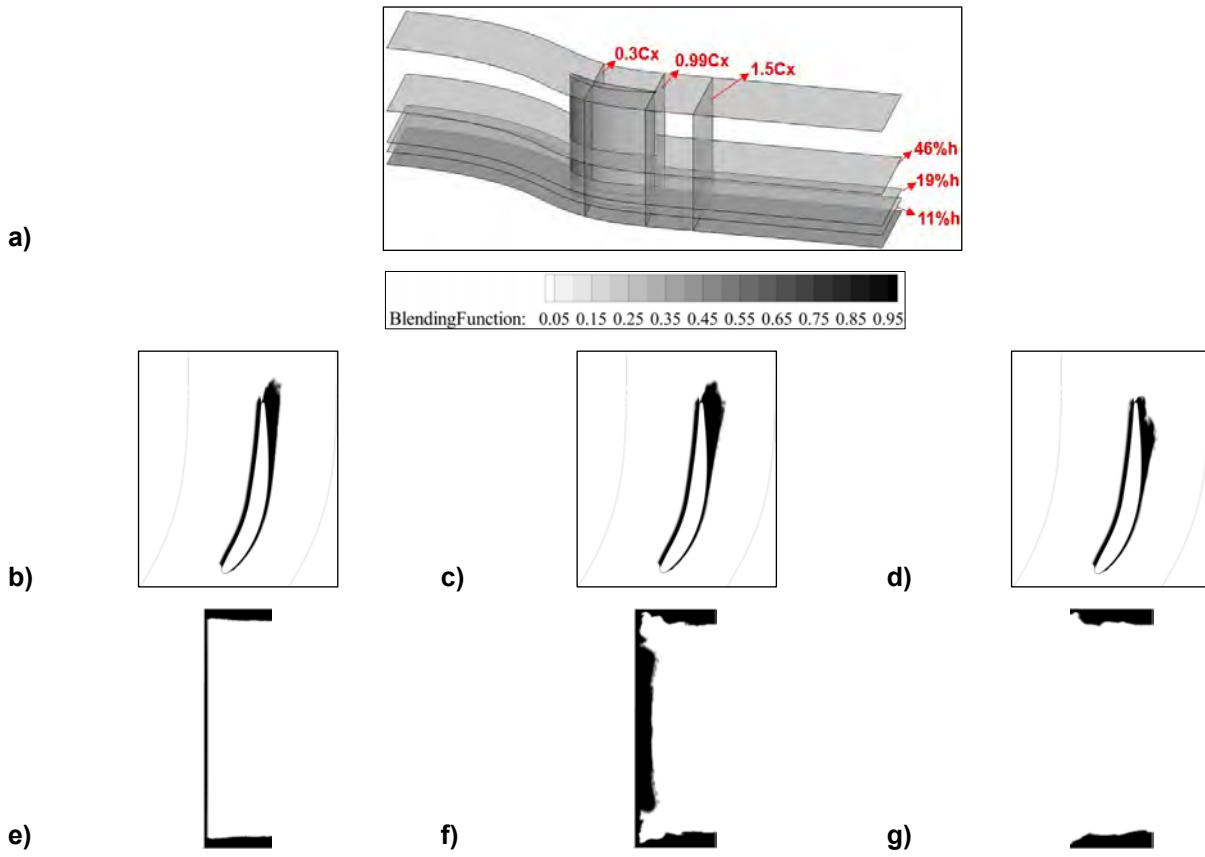


Figure 11: SBES blending function distribution (dark region: RANS; grey: RANS-LES; white: LES). (a) Location of cut planes, (b) 46%h, (c) 19%h, (d) 11%h, (e) 0.3Cx, (f) 0.99Cx, (g) 1.5Cx.

As a comparison between RANS and LES in terms of the numerical resolution of corner separation, Figure 12 shows the vortex structures given by RANS NSST and SBES-NSST-WALE. The brown region represents the vortex structures modelled by NSST while the light yellow one identifies the vortex structures resolved by the LES portion of SBES. The SBES aims to resolve the corner separation region where RANS models struggle to predict.

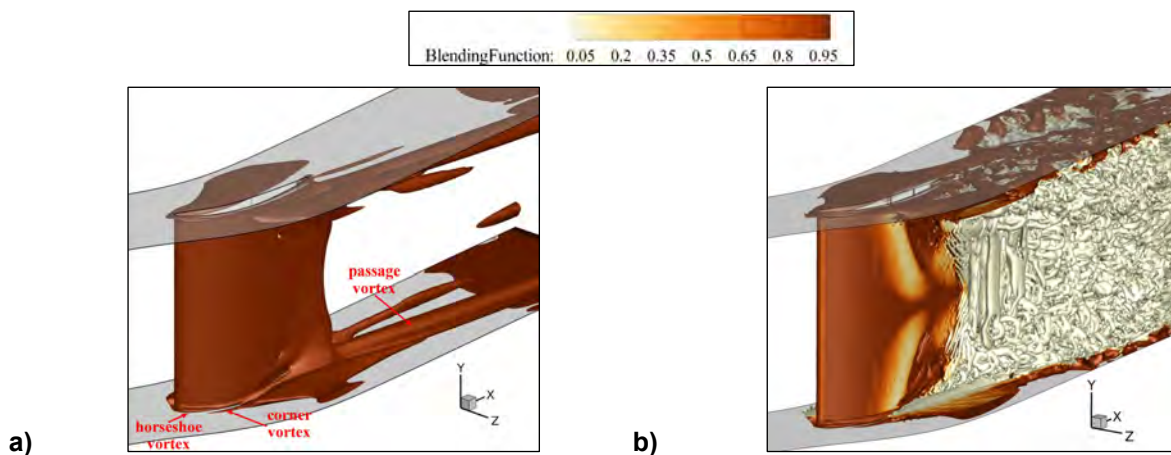


Figure 12: Iso-surfaces of Q criterion colored with the blending function ($Q=5,000s^{-2}$). (a) RANS NSST, (b) Instantaneous SBES-NSST-WALE.

As shown in Figure 12a, RANS captures some key turbulence structures in the endwall flow region: the leading-edge horseshoe vortex, the induced corner vortex downstream of the leading edge, and the skew-induced endwall secondary vortex. These turbulence structures are also observed in the instantaneous SBES flow field, as they are typically modelled by RANS. Once the flow separates, turbulence structures of various scales are resolved by LES (see in Figure 12b). The RANS-LES blending region is formulated along the separation lines, indicating smooth transition from RANS to LES.

Next, the time-averaged results of unsteady endwall flowfield are compared with the experimental results to validate SBES to predict the 3D separated flows. The prediction results of NSST-Helicity-QCR are also included to strengthen the claim on the general applicability of NSST-Helicity-QCR for the prediction of endwall separation in compressors.

Time-Averaged & NSST-Helicity-QCR Results

Figure 13 shows the blade pressure loading distributions predicted by SBES and NSST-Helicity-QCR model. It can be seen that closed corner separation is predicted by SBES, with turbulence scales resolved for enhanced mixing. Closed corner separation is given by NSST-Helicity-QCR as well, of which the results match closely with measurements.

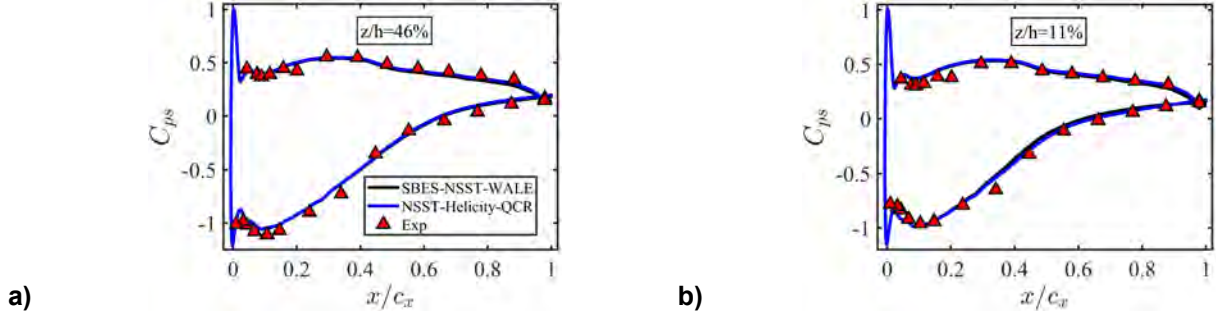


Figure 13: Blade spanwise C_{ps} distributions.

To quantify the extent of blockage due to separation, Figure 14a presents the distribution of the relative displacement thickness $\delta_r^*(y)$ across the blade trailing edge. It can be seen that SBES predicts “thicker” separated shear layer while the extent of blockage predicted by NSST-Helicity-QCR is “smaller” than measurements. In the region above $30\%h$, the blade boundary layer does not separate, of which the thickness predicted by NSST-Helicity-QCR corresponds well with measurements while SBES gives “thicker” boundary layer. However, the difference becomes more significant near the endwall where flow separates (below $15\%h$), and the reverse flow associated with corner separation exists. During the experimental measurement process, the hotwire was positioned normal to the flow (axial) direction at the trailing edge, and the axial velocities were recorded for data processing (Gbadebo, 2004). Unfortunately, the hotwire is unable to detect the reverse flow associated with separation, and thus the thickness of separation is underestimated. Therefore, it can be inferred that the time-averaged pitchwise extent of corner separation predicted by SBES matches closer to that of the “real” endwall separation, while a smaller corner separation is given by NSST-Helicity-QCR. This is consistent with the exit flow angle predictions at the measurement plane (see in Figure 14b).

Figure 14b shows the distribution of the pitchwise mass-averaged exit flow angle along the spanwise direction. It can be seen that SBES matches quite well with the experimental measurements, with the measurement uncertainty estimated to be $\pm 0.6^\circ$ (Gbadebo et al., 2005). In the region between $13\%h$ and mid-span, the predictions of SBES are within the measurement uncertainty while between $5\%h$ and $13\%h$, the predicted endwall blockage is more significant than the measured one. This shows consistency with the predicted pitchwise extent of blockage shown in Figure 14a. Given that the measurement uncertainty for the flow deviation near the endwall shall be larger than 0.6° , it is hard to quantify the deviation of the predicted exit flow angle from that of the real flow.

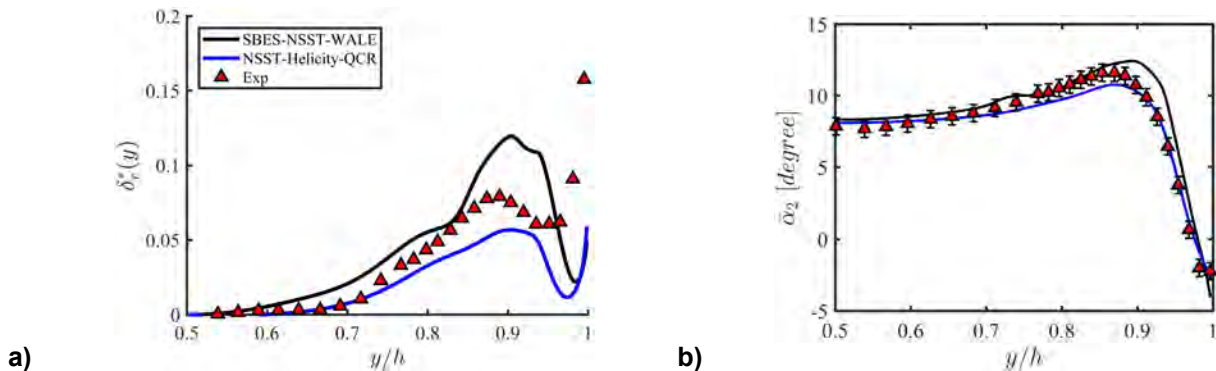


Figure 14: Metrics of the extent of corner separation. (a) Relative displacement thickness across the trailing edge, (b) Spanwise distribution of the pitchwise mass-averaged flow angle ($x=1.5c_x$).

In summary, both the SBES and the proposed NSST-Helicity-QCR model are validated against the endwall flow in a typical, high-loaded compressor cascade. For the blockage due to separation, the prediction results of SBES agree quite well with the experimental measurements, while a smaller extent of separation is predicted by NSST-Helicity-QCR in the pitchwise direction.

Turbulence Characteristics of 3D Endwall Flow

In this section, the SBES resolved turbulence database is used to study the turbulence characteristics of the endwall flow within the PVD compressor cascade. By analyzing the TKE budget terms and the anisotropic states of turbulence, the rationality of RANS model modifications in previous sections is strengthened.

Endwall Boundary Layer within the Blade Passage

To investigate the turbulence energy transport characteristics inside the endwall boundary layer, two positions within the blade passage were selected, and the wall-normal cut lines were placed at these positions to plot the distribution of TKE production along the endwall boundary layer. The selected positions are: location 1 (around the saddle point around the corner) and location 2 (downstream of the saddle point, which is outside the separation region), see in Figure 15.

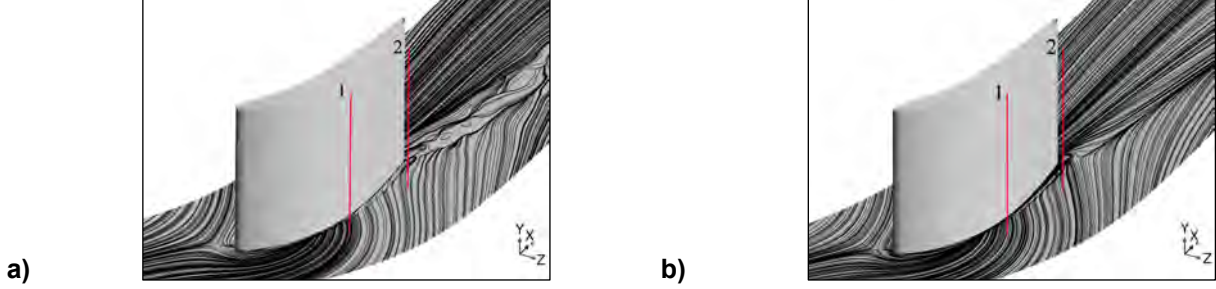


Figure 15: Endwall surface limiting streamlines, with cut lines positioned perpendicular to the endwall. (a) SBES-NSST-WALE, (b) NSST-Helicity-QCR.

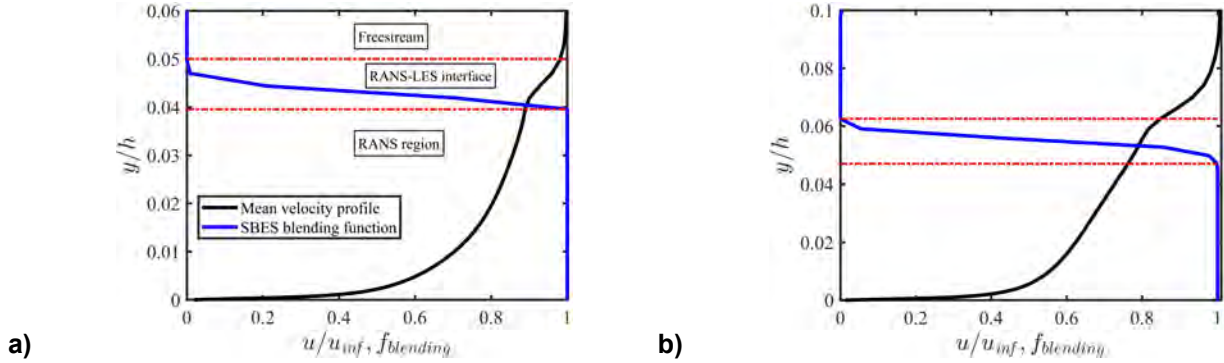


Figure 16: SBES blending function distribution along the endwall-normal cut line. (a) Location 1, (b) Location 2.

Figure 16 shows the mean velocity profile and the SBES blending function profile along the endwall boundary layer of location 1 and 2. It can be seen that at both locations, around 80% of attached boundary layer is covered by the RANS portion of SBES. In the region adjacent to the freestream (upper 20% layer region), the switchover from RANS to LES occurs, due to the low stress levels enforced by LES. In the freestream region, the flow is purely resolved by LES. Herein it can be understood as that the blending function enables most of attached boundary layers covered by RANS. It acts as an “identifier” of whether the flow is attached or not, and in the attached flow region, the performance comparison of SBES and RANS turns to be that of the RANS part of SBES (NSST) and NSST-Helicity-QCR.

Figure 17 shows the distribution of TKE production given by SBES and NSST-Helicity-QCR along the endwall boundary layer. The TKE production of SBES consists of two portions: modelled TKE production and resolved TKE production. The way of calculating modelled TKE production is the same as that using pure RANS/SGS model, with the expression listed as below:

$$(P_k)_{modelled} = \nu_t S^2 \quad (10)$$

where $(P_k)_{modelled}$ is the TKE production contributed from the modelled part of SBES, and ν_t is the RANS/SGS modelled eddy viscosity. The resolved TKE production is obtained from the scalar product of resolved Reynolds stress tensor and resolved mean velocity gradient tensor, which is expressed as:

$$(P_k)_{resolved} = -\overline{u_i u_j} \frac{\partial u_i}{\partial x_j} \quad (11)$$

The total TKE production given by SBES is:

$$(P_k)_{SBES} = (P_k)_{modelled} + (P_k)_{resolved} \quad (12)$$

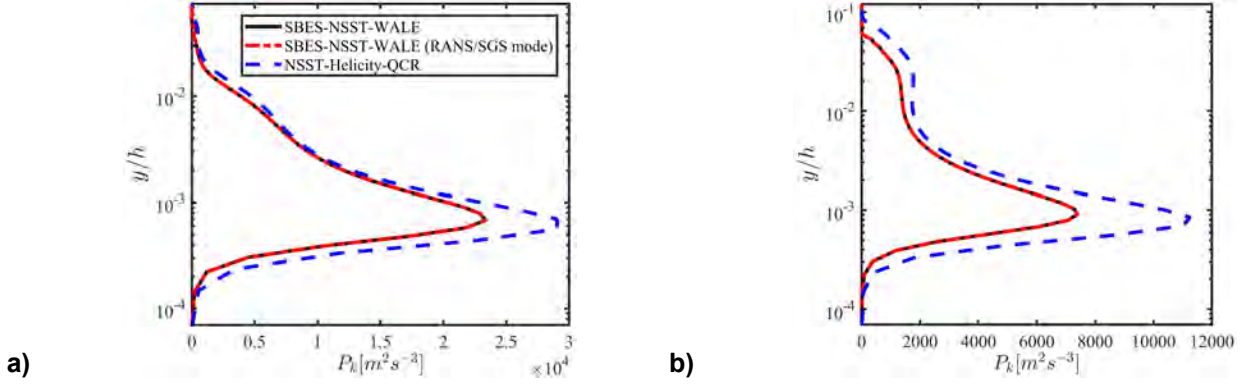


Figure 17: Distribution of P_k along the endwall boundary layer. (a) Location 1, (b) Location 2.

Along the endwall boundary layer of both location 1 and 2, the distribution of the SBES TKE production contributed by the RANS portion of SBES (NSST) overlaps that of the overall SBES TKE production. This supports the conclusion drawn from Figure 16 that in SBES, most the attached endwall boundary layer is covered by RANS, and in the near-wall RANS-LES interface zone, RANS still dominates, due to the grid too coarse to sustain resolved turbulence. Furthermore, a combined QCR and helicity modifications to the NSST model (NSST-Helicity-QCR) results in higher TKE production inside the endwall boundary layer than NSST does. Given that the endwall boundary layer predicted by NSST is strong enough to migrate down to the endwall-suction surface corner, it is no surprise that NSST-Helicity-QCR gives a similar endwall boundary layer state (see in both subfigures in Figure 15).

Separated Shear Layer around the Corner Region

Once flow separates, a strong shear interaction with the main passage flow exists in the outer layer of separated shear layer, indicating high TKE generated in that area. By plotting the distribution of TKE budget terms within the separation region, the outer layer position can be identified, and the corner separation size can be determined.

Figure 18 shows the distribution of TKE production predicted by SBES and NSST-Helicity-QCR along the selected blade surface-normal cut line. It can be shown in Figure 18b that the location of maximum P_k given by the SGS model is almost the same as the location by LES, indicating highest strain rates existing in the outer layer (see in Equation (10) and (11)). Furthermore, the maximum P_k location given by NSST-Helicity-QCR is quite close (more precisely, slightly closer to the blade surface) to the time-averaged solution of the SBES resolved corner separation. This is regarded as the physical reason for the “thinner” separated shear layer predicted by NSST-Helicity-QCR, compared with that by SBES and the experimental measurements (see in Figure 14a).

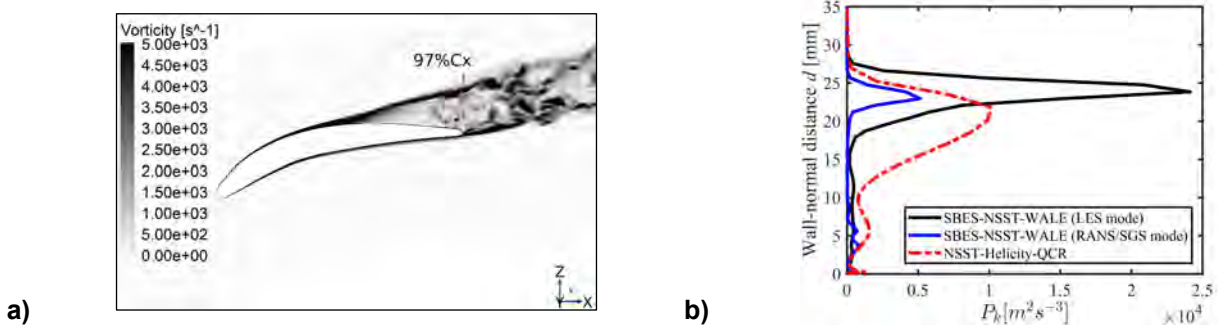


Figure 18: Distribution of P_k along the blade surface-normal cut line. (a) Vorticity magnitude contour at 9%h, with location of cut line normal to the suction surface, (b) P_k distribution.

Based on the above analysis, it can be concluded that by modifying the turbulence production source terms based on the turbulence transport nature of endwall flow, NSST-Helicity-QCR model better captures the non-equilibrium endwall flow physics, thus obtaining improved corner separation prediction.

Next, the turbulence anisotropic characteristics within corner separation is investigated to evaluate the capability of NSST-Helicity-QCR model to reproduce the anisotropic corner flow physics.

The anisotropic turbulence state is visualized using the anisotropic invariant maps. Originally introduced by Lumley and Newman (1977), these maps are 2D domains based on invariant properties of the Reynolds stress anisotropy tensor a_{ij} , with a_{ij} expressed as:

$$a_{ij} = \frac{\overline{u_i u_j}}{2k} - \frac{1}{3} \delta_{ij} \quad (13)$$

The second-order anisotropy tensor a_{ij} has three scalar invariants. For incompressible flows, the first invariant equals 0, and the second invariant η and third invariant ζ are expressed as (Lumley and Newman, 1977):

$$6\eta^2 = a_{ij}a_{ji} \quad (14)$$

$$6\zeta^3 = a_{ij}a_{jk}a_{ki} \quad (15)$$

Statistic evaluation of turbulence anisotropy can be done by plotting η and ζ on Lumley triangle map, in which the boundaries represent the three limiting states of turbulence (see in Figure 19). For example, the origin (0,0) represents the isotropic state of turbulence. All other turbulence states (other locations in the Lumley triangle map) can be represented as convex combinations of these limiting states.

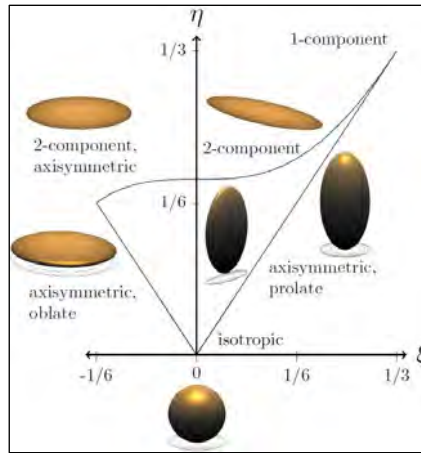


Figure 19: Sketch of the Lumley & Newman anisotropic invariant map (Lumley & Newman, 1977).

Figure 20 shows the evolution of the anisotropic turbulence states along the blade surface-normal cut line shown in Figure 18a. As shown from the SBES results, large turbulence anisotropy exists across the separated shear layer. Along the cut line from the blade surface outwards, turbulence state changes from the axisymmetric “2-component” turbulence to the “axisymmetric prolate” shape, and then switches between the “axisymmetric prolate” shape and the “axisymmetric oblate” shape.

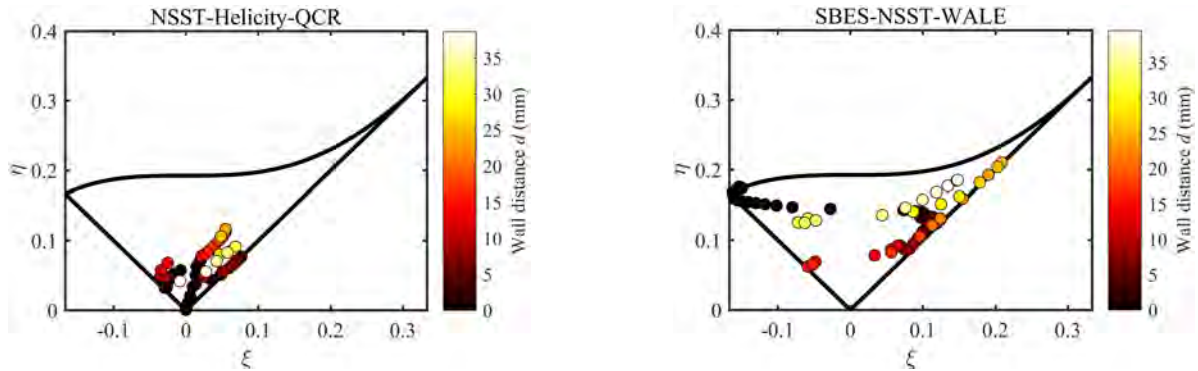


Figure 20: Evolution of turbulence anisotropy along the blade surface-normal cut line.

In contrast, despite it being improved by QCR correction, turbulence anisotropy is still being suppressed by NSST-Helicity-QCR, which is embodied in the nearly isotropic states of turbulence predicted across the separation region. As the non-equilibrium turbulence behaviours inside the endwall boundary layer impact more on the endwall secondary flow development within the PVD cascade passage (see in Figure 17), NSST-Helicity-QCR still gives reasonable results (see in Figure 15). However, for the LMFA-NACA65 cascade flow, the underestimation of turbulence anisotropy has a more significant negative impact on corner separation predictions (see for example in Figure 7). In the next research phase, improvement of the NSST-Helicity-QCR model will be carried out by further studies of the SBES turbulence database.

CONCLUSIONS

In the present research, Menter’s SST model, which has been widely used in turbomachinery communities, is used as a benchmark turbulence model to investigate the effects of the turbulence non-equilibrium and anisotropic modifications on the prediction of the compressor endwall separation. Three model modifications, i.e., stress limiter switch-off, velocity helicity correction, and explicit quadratic Reynolds stress-strain constitutive relation, are adopted as extension of the SST

model. The first two are in the context of the non-equilibrium modification while the third is one type of the anisotropic modification. The validation results demonstrate that each modification captures part of the endwall flow physics, such as skew-induced turbulence non-equilibrium, turbulence energy backscatter, and turbulence anisotropy caused by 3D shear skewing, so as to improve the prediction accuracy of corner separation.

However, the compressor endwall flow is a complex physical phenomenon in which the turbulence non-equilibrium, anisotropy and energy backscatter coexist. This inspires the author to synthesize the isolated modifications and propose a new model named NSST-Helicity-QCR. The model validation results demonstrate its significantly better performance in predicting corner separation and the resulting impact on compressor performance.

Finally, to add strength to the statement that NSST-Helicity-QCR model indeed captures more of the endwall flow physics, a high-fidelity SBES turbulence database is used to feedback on RANS modelling. It is found that in the endwall boundary layer which is upstream of corner separation, the turbulence non-equilibrium predicted by NSST-Helicity-QCR is more significant than that by SBES. The turbulence energy production of NSST-Helicity-QCR is higher, and thus the endwall boundary-layer fluid is energised to be more resistant to separation. In the corner separation region, the location of maximum TKE production predicted by NSST-Helicity-QCR is close to that by SBES, indicating the extent of corner separation being reasonably modelled. However, the turbulence anisotropy in corner separation is still underestimated by the QCR portion of NSST-Helicity-QCR. Future research will focus on improving NSST-Helicity-QCR model by further studies of the scale-resolving flow solutions.

NOMENCLATURE

C_{ps}	static pressure coefficient, $(p-p_1)/(p_{01}-p_1)$
C_{pt}	total pressure loss coefficient, $(p_{01}-p_0)/(p_{01}-p_1)$
h	absolute value of the relative helicity density/blade span
i	inlet incidence angle, degree
p	local static pressure, Pa
p_0	local total pressure, Pa
p_1	inlet endwall static pressure, Pa
p_{01}	inlet freestream total pressure, Pa
α	flow angle, degree
δ^*	boundary layer displacement thickness, m
$\bar{\varphi}$	mass-weighted average of φ

ACKNOWLEDGMENTS

Herein, the author expresses gratitude to Dr. Jiahuan Cui of Zhejiang University for his advice on generation of the LES-type mesh and the valuable discussions during paper drafting. Anonymous reviewers are also appreciated for their unreserved comments and suggestions.

REFERENCES

- Bush, R. H., Chyczewski, T. S., Duraisamy, K., Eisfeld, B., Rumsey, C. L., & Smith, B. R. (2019). Recommendations for Future Efforts in RANS Modeling and Simulation. In *AIAA Scitech 2019 Forum*, p. 0317.
- Denton, J. D. (2010, October). Some Limitations of Turbomachinery CFD. In *Turbo Expo: Power for Land, Sea, and Air*, Vol. 44021, pp. 735-745. American Society of Mechanical Engineers Digital Collection.
- Ducros, F., Nicoud, F., & Poinso, T. (1998). Wall-Adapting Local Eddy-Viscosity Models for Simulations in Complex Geometries. *Numerical Methods for Fluid Dynamics VI*, pp. 293-299.
- Gbadebo, S. A. (2004). *Three-dimensional separations in compressors*. Ph.D. University of Cambridge.
- Gbadebo, S. A., Cumpsty, N. A., & Hynes, T. P. (2005). Three-Dimensional Separations in Axial Compressors. *Journal of Turbomachinery*, 127(2), pp. 331-339.
- Gbadebo, S. A., Cumpsty, N. A., & Hynes, T. P. (2007). Interaction of Tip Clearance Flow and Three-Dimensional Separations in Axial Compressors. *Journal of Turbomachinery*, 129(4), pp. 679-685.
- Goodhand, M. N., & Miller, R. J. (2011). Compressor Leading Edge Spikes: a New Performance Criterion. *Journal of turbomachinery*, 133(2).
- Gourdain, N., Sicot, F., Duchaine, F., & Gicquel, L. (2014). Large Eddy Simulation of Flows in Industrial Compressors: a Path from 2015 to 2035. *Philosophical Transactions of the Royal society A: Mathematical, Physical and engineering sciences*, 372(2022): 20130323.
- Liu, Y., Lu, L., Fang, L., & Gao, F. (2011). Modification of Spalart–Allmaras Model with Consideration of Turbulence Energy Backscatter Using Velocity Helicity. *Physics Letters A*, 375(24), pp. 2377-2381.
- Liu, Y., Tang, Y., Scillitoe, A. D., & Tucker, P. G. (2019). Modification of Shear Stress Transport Turbulence Model Using Helicity for Predicting Corner Separation Flow in a Linear Compressor Cascade. *Journal of Turbomachinery*, 142(2).

- Lumley, J. L., & Newman, G. R. (1977). The Return to Isotropy of Homogeneous Turbulence. *Journal of Fluid Mechanics*, 82(1), pp. 161-178.
- Ma, W. (2012). *Experimental Investigation of Corner Stall in a Linear Compressor Cascade*. Ph.D. École Centrale de Lyon.
- Ma, W., Ottavy, X., Lu, L., Leboeuf, F., & Gao, F. (2011). Experimental Study of Corner Stall in a Linear Compressor Cascade. *Chinese Journal of Aeronautics*, 24(3), pp. 235-242.
- Menter, F. R. (1994). Two-Equation Eddy-Viscosity Turbulence Models for Engineering Applications. *AIAA Journal*, 32(8), pp. 1598-1605.
- Menter, F. R. (2015). Best Practice: Scale-Resolving Simulations in ANSYS CFD. *ANSYS Germany GmbH*, 2.
- Menter, F. R. (2016, September). Stress-Blended Eddy Simulation (SBES)—A New Paradigm in Hybrid RANS-LES Modeling. In *Symposium on Hybrid RANS-LES methods*, pp. 27-37. Springer, Cham.
- Menter, F. R., Kuntz, M., & Langtry, R. (2003). Ten Years of Industrial Experience with the SST Turbulence Model. *Turbulence, heat and mass transfer*, 4(1), pp. 625-632.
- Menter, F. R., Matyushenko, A., & Lechner, R. (2018, November). Development of a Generalized k- ω Two-Equation Turbulence Model. In *Symposium der Deutsche Gesellschaft für Luft-und Raumfahrt*, pp. 101-109. Springer, Cham.
- Spalart, P. R. (2009). Detached-Eddy Simulation. *Annual review of fluid mechanics*, 41, pp. 181-202.
- Sun, W. (2021). *Turbulence Modelling for Complex Flows in Turbomachinery*. Ph.D. University of Cambridge.
- Sun, W., & Xu, L. (2021). Improvement of Corner Separation Prediction Using an Explicit Non-Linear RANS Closure. *Journal of the Global Power and Propulsion Society*, 5, pp. 50-65.
- Sun, W., Wang, Z. -N., & Xu, L. (2020, September). Numerical Resolution of Compressor Corner Separation Problem. In *ASME Turbo Expo 2020: Turbomachinery Technical Conference and Exposition*, Vol. 2C, p. V02CT35A013. American Society of Mechanical Engineers Digital Collection.
- Wang, Z. -N., & Yuan, X. (2013, June). Unsteady Mechanisms of Compressor Corner Separation Over a Range of Incidences Based on Hybrid LES/RANS. In *Turbo Expo: Power for Land, Sea, and Air*, Vol. 55225, p. V06AT35A030. American Society of Mechanical Engineers Digital Collection.
- Zambonini, G. (2016). *Unsteady Dynamics of Corner Separation in a Linear Compressor Cascade*. Ph.D. École Centrale de Lyon.
- Zambonini, G., Ottavy, X., & Kriegseis, J. (2017). Corner Separation Dynamics in a Linear Compressor Cascade. *Journal of Fluids Engineering*, 139(6).